Title
Quantification of the loss mechanisms in emerging water splitting photoanodes through empirical extraction of the spatial charge collection efficiency

Journal
Energy & Environmental Science, 11(4)

ISSN
1754-5692

Authors
Segev, Gideon
Jiang, Chang-Ming
Cooper, Jason K
et al.

Publication Date
2018

DOI
10.1039/c7ee03486e

Peer reviewed

Energy & Environmental Science

PAPER

View Article Online
View Journal

Cite this: DOI: 10.1039/c7ee03486e

Quantification of the loss mechanisms in emerging water splitting photoanodes through empirical extraction of the spatial charge collection efficiency†

Gideon Segev, [ab] Chang-Ming Jiang, [ab] Jason K. Cooper, [ab] Johanna Eichhorn,[ab] Francesca M. Toma [ab] and Ian D. Sharp *[abc]

Received 8th December 2017,
Accepted 13th February 2018

DOI: 10.1039/c7ee03486e

rsc.li/ees

The *operando* quantification of surface and bulk losses is key to developing strategies for optimizing photoelectrodes and realizing high efficiency photoelectrochemical solar energy conversion systems. This is particularly true for emerging thin film semiconductors, in which photocarrier diffusion lengths, surface and bulk recombination processes, and charge separation and extraction limitations are poorly understood. Insights into mechanisms of efficiency loss can guide strategies for nanostructuring photoelectrodes, engineering interfaces, and incorporating catalysts. However, few experimental methods are available for direct characterization of dominant loss processes under photoelectrochemical operating conditions. In this work, we provide insight into the function and limitations of an emerging semiconductor photoanode, γ-$Cu_3V_2O_8$, by quantifying the spatial collection efficiency (SCE), which is defined as the fraction of photogenerated charge carriers at each point below the surface that contributes to the measured current. Analyzing SCE profiles at different operating potentials shows that increasing the applied potential primarily acts to reduce surface recombination rather than to increase the thickness of the space charge region under the semiconductor/electrolyte interface. Comparing SCE profiles obtained with and without a sacrificial reagent allows surface losses from electronically active defect states to be distinguished from performance bottlenecks arising from slow reaction kinetics. Combining these insights promotes a complete understanding of the photoanode performance and its potential as a water splitting photoanode. More generally, application of the SCE extraction method can aid in the discovery and evaluation of new materials for solar water splitting devices by providing mechanistic details underlying photocurrent generation and loss.

Broader context

The next generation of solar energy conversion systems require design and integration of new semiconductor materials. Detailed understanding of the opto-electronic properties of these materials and the driving forces and loss mechanisms that limit device performance is essential to the development of high efficiency systems. Insights into mechanisms of efficiency loss can guide strategies for nanostructuring photoelectrodes, engineering interfaces, and incorporating catalysts. However, few experimental methods are available for direct characterization of dominant loss processes under photoelectrochemical operating conditions. In this work, we provide insight into the function and limitations of an emerging semiconductor photoanode, γ-$Cu_3V_2O_8$, by quantifying the spatial collection efficiency (SCE), which is defined as the fraction of photogenerated charge carriers at every point that contribute to extracted current. Analyzing SCE profiles at different operating potentials while performing different chemical reactions allows distinguishing between bulk and surface losses and between different types of surface recombination mechanisms. Combining these insights promotes a complete understanding of the photoanode performance and its potential as a water splitting photoanode. More generally, application of the SCE extraction method can aid in the discovery and evaluation of new materials for solar water splitting devices by providing mechanistic details underlying photocurrent generation and loss.

[a] *Chemical Sciences Division, Lawrence Berkeley National Laboratoy, Berkeley, CA 94720, USA*
[b] *Joint Center for Artificial Photosynthesis, Lawrence Berkeley National Laboratoy, Berkeley, CA 94720, USA*
[c] *Walter Schottky Institut and Physik Department, Technische Universität München, 85748 Garching, Germany. E-mail: sharp@wsi.tum.de*

† Electronic supplementary information (ESI) available. See DOI: 10.1039/c7ee03486e

Introduction

Photoelectrochemical (PEC) conversion of solar energy provides a promising approach to generating renewable and sustainable fuels but requires semiconductors that can support high efficiency, are robust under operating conditions, and can be scaled

to meet the global energy challenge. Currently, there remains a lack of materials that can simultaneously meet all of these requirements. Therefore, considerable effort is aimed at the discovery and development of new semiconductor photoelectrodes. Candidate materials are usually identified based on their bandgaps and stabilities in aqueous environments. However, extensive work is also required to characterize their electronic and catalytic properties in order to identify specific performance bottlenecks and loss mechanisms. This is a key step in determining the true potential of emerging materials and guiding strategies for optimizing their functionality.[1,2]

An outstanding challenge in the pursuit of new semiconductor photoelectrodes is the lack of a single, nondestructive, and *operando* technique for quantifying all efficiency loss mechanisms, while also distinguishing between bulk and surface recombination. The emergence of such a technique could significantly accelerate device and material development by providing insights into how bulk transport, photocarrier recombination, and surface chemical reaction govern performance characteristics under real operating conditions. In this work, we show that simple experimental techniques can be used to extract the spatial collection efficiency,[3–9] $\phi(z)$, thereby allowing different loss mechanisms in an emerging semiconductor photoanode material, γ-$Cu_3V_2O_8$, to be probed and quantified. Defined as the fraction of optically generated charge carriers at a given location that contribute to the chemical reaction, the spatial collection efficiency (SCE) provides a functional depth profile of the active regions in the device. The $\phi(z)$ profile extracted in the presence of a sacrificial reagent yields additional information about fast recombination events at electronically active defects on the photoelectrode surface that are not probed by other methods. Finally, a comparison between $\phi(z)$ profiles obtained with and without a sacrificial reagent gives information on the injection efficiency at the surface, thus allowing a complete portrait of loss and transport mechanisms in the photoelectrode to be drawn.

To date, most of the methods used in photoelectrochemistry can only probe surface losses attributed to slow reaction kinetics. For example, photocurrent *vs.* electrochemical potential (J–E) curves obtained in the presence and absence of a sacrificial reagent,[10,11] transient photocurrent spectroscopy[12,13] and frequency domain techniques such as impedance spectroscopy and intensity modulated photocurrent spectroscopy[14–17] provide information on relatively slow surface recombination events at the electrode surface. While these analyses are very effective in describing the reaction rate quantitatively, they rely on a simplified description of charge transport mechanisms and transfer pathways, thus convoluting together the effects of several processes. For this reason, and because of the extremely short time constants involved in bulk charge transport, such techniques hold little information about the bulk processes and cannot distinguish between bulk loss mechanisms and surface recombination events occurring at electronically active surface defect states.

Quantification of the minority carrier diffusion length in newly discovered thin film materials also proves challenging. This is particularly true for transition metal oxides and oxynitrides, which are intensively investigated for application in photoelectrochemical energy conversion but usually do not exhibit band-edge luminescence. As such, a broad range of the techniques developed for characterization of technologically important III–V materials are not applicable to many of these emerging semiconductor compounds.[18,19] In addition, electron beam induced current (EBIC), as described in ref. 20–23, requires fabrication of full device stacks that are measured under vacuum, which prohibits use of this method for characterization of photoelectrochemical systems under real operating conditions. To overcome this characterization gap and extract the diffusion length, Pala *et al.*[24] suggested measuring photocurrent changes in wedge-shaped thin films. However, such geometries are difficult to fabricate and their behavior may deviate significantly from the performance of planar structures.

Extraction of the SCE offers a non-destructive, *operando* method to evaluate and quantify the transport and loss mechanisms in new materials.[3–9] The method couples optical modelling based on data obtained from spectroscopic ellipsometry with incident photon-to-current efficiency (IPCE) measurements. As a recently discovered material system for water splitting, copper vanadate[25–28] serves as an excellent case study for the suggested method. Although γ-$Cu_3V_2O_8$ has a rather narrow band gap and excellent stability, the photocurrent harvested from it falls far below the theoretical values. Furthermore, unlike materials such as hematite, where some absorbed photons do not generate mobile charge carriers,[9,29] the spectral separation between d–d transitions and band-to-band transitions[30] reduces the complexity of the analysis considerably. In this work, we show that nearly 98% of the charge carriers generated within the photoanode are lost through bulk recombination. However, when increasing the applied potential, the increase in photocurrent is predominantly a result of improved surface properties rather than charge collection from deeper regions within the device. By comparing spatial collection efficiency profiles with and without a sacrificial reagent, fast surface recombination losses through electronically active defect states can be discriminated from surface losses due to poor catalytic activity. These results reveal specific strategies for surface passivation, doping, and catalyst incorporation that may be used to improve the functional characteristics of this newly identified photoanode material. The simple experimental apparatus required for this method and the wealth of information obtained by it are expected to help accelerate the search for new solar energy materials, assess the potential of these compounds as next-generation photoelectrodes, and develop strategies for increasing performance *via* interface engineering, nanostructuring, and light management.

Analysis

The spatial collection efficiency (SCE) is defined as the fraction of charge carriers that are photogenerated at a specific point within the device that contribute to the measured current. Since the measured current can be used to produce electrical power or run a chemical reaction, the following derivation

holds for both photovoltaic and photoelectrochemical cells. In such systems, the photocurrent density, J_{photo}, follows:[3–9]

$$J_{photo} = q\int_0^d G(z)\phi(z)\mathrm{d}z \quad (1)$$

where q is the electron charge, d is the absorber thickness, and $G(z)$ is the optical generation at a depth, z, from the illuminated interface. For the case of PV cells, Sinkkonen *et al.* suggested that the $\phi(z)$ profile could be extracted by combining optical modeling and external quantum efficiency (EQE), or equivalently, incident photon-to-current efficiency (IPCE), measurements.[3,4] In these measurements, the photocurrent density is measured as a function of an incident monochromatic illumination wavelength, λ, and can be expressed as:

$$\Delta J_{photo}(\lambda) = q\int_0^d \Delta G(\lambda, z)\phi(z)\mathrm{d}z \quad (2)$$

Here, $\Delta J_{photo}(\lambda)$ is the current response to monochromatic illumination and $\Delta G(\lambda,z)$ is the optical generation induced by the monochromatic light. It should be noted that, in many cases, IPCE measurements are conducted with a background white light bias applied to the device. However, only the optical generation and current responses associated with the monochromatic input should be inserted into eqn (2). In their work, Sinkkonen *et al.* assumed a thick silicon solar cell in which the optical generation profile decays exponentially with depth at every wavelength. This allows solving for $\phi(z)$ simply by plotting ΔJ_{photo} as a function of the absorption coefficient at every wavelength and performing a reverse Laplace transform on the resulting curve. Donolato extracted the collection efficiency profiles out of published spectral responses of silicon and InP solar cells using a deconvolution method that also assumed a Beer–Lambert like optical absorption.[6] However, thin films and heterojunctions, such as those commonly used for PEC applications, cannot be assumed to have exponentially decaying optical generation profiles. Hence, the suggested method has to be refined to accept arbitrary optical generation profiles. Pang *et al.*[5] and Segev *et al.*[9] suggested solving eqn (2) using standard regularization methods, such as Tichonov,[31,32] and applied it to CIGS solar cells[5] and hematite water splitting photoanodes, respectively.[9] In order to apply such methods, eqn (2) must be discretized:

$$\Delta J_{photo}(\lambda_i) = q \cdot \Delta\overline{\overline{G'}}(\lambda, z_i)\phi(z_i) \quad (3)$$

In this case, the device is divided into finite, 1D spatial elements of various widths such that $\Delta\overline{\overline{G'}}(\lambda, z_i)$ has units of $\mathrm{cm}^{-2}\ \mathrm{s}^{-1}$ and is a matrix describing the total optical generation within the i^{th} element located at position z_i induced by monochromatic illumination with wavelength λ_i. $\Delta J_{photo}(\lambda_i)$ is the corresponding vector of measured photocurrent densities. In the regularization process, the measured IPCE data, $\Delta J_{photo}(\lambda_i)$ and the modeled optical generation profile, $\Delta\overline{\overline{G'}}(\lambda, z_i)$, are inserted into eqn (4), where the extracted collection efficiency vector, $\phi(z_i)$, minimizes the norm, ε[31,32]:

$$\varepsilon = \left\| q \cdot \Delta\overline{\overline{G'}}(\lambda, z_i)\phi(z_i) - \Delta J_{photo}(\lambda_i) \right\|_2 \quad (4)$$

It should be noted that in many cases, such regularization problems are ill posed and have an infinite number of solutions, of which only one is the physical solution. Methods for obtaining the physical solution by applying appropriate constraints can be found in ref. 9, 31 and 32 and in the ESI.† All collection efficiency profiles were extracted using the discrete regularization process described by eqn (4). However, for the sake of simplicity, the notation $\phi(z)$ is used throughout the remainder of the text to describe the spatial collection efficiency.

Loss quantification

The collection efficiency can be divided into a bulk component, $\phi_b(z)$, which denotes the efficiency at which charge carriers generated at point, z, reach the surface, and the interfacial charge transfer efficiency, ϕ_s, which is the probability for charge carriers to be injected across surfaces and interfaces. For the case of photoelectrochemical systems, such as the one investigated here, this quantity represents the surface reactivity, defined as the probability that charge carriers that reach the surface contribute to the reaction. Thus, the total charge collection efficiency can be expressed as:

$$\phi(z) = \phi_s \cdot \phi_b(z) \quad (5)$$

In minority carrier transport limited photoelectrodes, such as γ-$Cu_3V_2O_8$ or hematite, and assuming no geminate recombination, ϕ_b can be assumed to be 1 at the surface. Hence, ϕ_s is the value of the extracted SCE at $z = 0$ and $\phi_b(z) = \phi(z)/\phi_s$. However, this is not necessarily the case for all photoelectrodes or solar cells. Further discussion about this assumption can be found in the ESI.† In order to quantify the losses associated with the bulk and surfaces, the integrated bulk collection probability can be defined as:

$$\bar{\phi}_b = \frac{\frac{1}{\phi_s}\int_0^d G(z)\phi(z)\mathrm{d}z}{\int_0^d G(z)\mathrm{d}z} \quad (6)$$

The integrated bulk loss, $\bar{R}_b = 1 - \bar{\phi}_b$, marks the fraction of photogenerated charge carriers that recombine anywhere in the bulk of the photoanode and the surface loss, $\bar{R}_s$, denotes the fraction of all photogenerated charge carriers that reach the surface but do not contribute to the chemical reaction, according to:

$$\bar{R}_s = \bar{\phi}_b(1 - \phi_s) \quad (7)$$

The integrated collection efficiency, $\bar{\phi}$, follows

$$\bar{\phi} = \bar{\phi}_b\phi_s \quad (8)$$

Hence, for a given optical generation profile, eqn (6)–(8) can be used to quantify the fraction of the overall generated charge carriers that are collected (*i.e.*, participate in chemical reaction for the case of photoelectrochemical systems), lost to surface recombination, or lost to bulk recombination. Setting $G(z)$ to be the optical generation profile produced by the AM 1.5G spectrum is the natural choice for analyzing these metrics, though is not a strict requirement if, for example, the bottom electrode of a tandem photoelectrochemical device is to be evaluated.

Methods

External quantum efficiency measurement and incident photon-to-current efficiency measurements

External quantum efficiency (EQE)/incident photons-to-current efficiency (IPCE) measurements were carried out using a Newport 300 W ozone-free Xe lamp, whose optical output was passed through an Oriel Cornerstone 130 1/8 m monochromator. The sample current was measured with a Gamry Reference 600 potentiostat. The monochromatic light was stepped in 5 nm intervals and chopped at a period between 1 and 4 s depending on the settling time of the current signal. A Mightex GCS-6500-15-A0510 light emitting diode and a Mightex LGC-019-022-05-V collimator were used to produce the background light bias. The LED current was set to 50 mA which yields an optical output that is significantly lower than 1 Sun but is about 20 times larger than the monochromatic signal, thus permitting an acceptable signal to noise ratio and minimizing heating effects. The relevant photocurrent was calculated by subtracting the current generated under background light illumination from the current generated in the presence of both monochromatic and background light illumination. The incident optical output at each wavelength was measured with a Thorlabs SM05PD2A photodiode. The photodiode was calibrated using a Newport 818-UV/DB calibrated detector.

Optical characterization

Transmission and reflectance measurements were taken with a Shimadzu SolidSpec-3700 UV/Vis/NIR spectrometer using an integrating sphere. The baseline for the reflectance measurement was collected with an Ocean Optics STAN-SSH-NIST NIST traceable reference mirror.

Variable angle spectroscopic ellipsometry measurements were conducted between 45–75° in 5° increments, as well as in transmission geometry at an incident angle of 90°, with a spectral range of 192–1690 nm using a J. A. Woollam Co. M-2000DI spectroscopic ellipsometer. The reflection intensity was calibrated against a known Si/SiO_2 standard. The optical constants for each of the layers were extracted independently. The glass substrate data was collected by etching the ITO off the ITO-coated glass substrate. An optical model was then developed for ITO on glass and for ITO on glass after annealing at 550 °C (similar to the post deposition annealing conditions). Finally, the optical constants of the fully prepared γ-$Cu_3V_2O_8$ sputtered on ITO coated glass were extracted. Oscillator-based optical models were fixed for the glass and annealed ITO and a b-spline model with Kramers–Konig restrictions was fitted for the γ-$Cu_3V_2O_8$ layer. Fitting was done for both the variable angle spectroscopic ellipsometry reflection intensity and transmission intensities concurrently. Slight variations in the layer composition during the γ-$Cu_3V_2O_8$ layer growth were accounted for by introducing a graded optical model to this layer (5 layers of equal thickness).

Optical modelling

The optical properties and optical generation profiles for the γ-$Cu_3V_2O_8$ photoanode were modeled using the Transfer Matrix Method, which accounts for thin film interference patterns within the cell assuming perfectly flat one dimensional structures.[33] Multiple reflections in incoherent layers such as the quartz window, water layer, and glass substrate were accounted for using the phase elimination method as described in ref. 34. The thickness of the γ-$Cu_3V_2O_8$ and ITO layers was estimated by comparing the computed transmission and reflection spectra to the UV-Vis results.

γ-$Cu_3V_2O_8$ deposition

Thin films of γ-$Cu_3V_2O_8$ were deposited by radio frequency magnetron co-sputtering of Cu and V metal targets onto 50 × 75 mm^2, 1.1 mm thick indium tin oxide (ITO) coated glass substrates (CB-50IN-S211, Delta Technologies) in a sputtering deposition system (LAB Line, Kurt J. Lester). The reactive working atmosphere consisted of 10 mTorr of inert Ar and 1 mTorr of O_2, and the substrate temperature was kept at 400 °C during the process. The powers on the metal targets were 22 and 260 W for Cu and V, respectively. After 120 min of sputtering, the as-deposited film was then annealed in air at 550 °C for 1 h with a 12 °C min^{-1} ramp, followed by natural cooling to room temperature. More details about the structural and compositional characterization of the γ-$Cu_3V_2O_8$ layers can be found in ref. 30.

SCE extraction

The SCE profiles were extracted out of the IPCE spectra and optical generation profiles were computed using the Matlab regularization tool box.[32] At a first stage, the generalized singular value decomposition (SVD) was computed for the optical generation matrix $\Delta\overline{\overline{G'}}(\lambda, z_i)$ assuming second derivative constraints. Next, an L-curve was produced using a damped SVD (DSVD) algorithm and a very wide range of regularization parameters from which the regularization parameter corresponding to the knee of the curve, κ_{knee}, was extracted. Once the knee of the L-curve was identified, a set of solutions corresponding regularization parameters in the range $0.1\kappa_{knee} \leq \kappa \leq 10\kappa_{knee}$ were computed and averaged at every value of z to produce the averaged SCE profile. More details regarding the numerical procedure and a discussion of the choice of grid used can be found in the ESI.†

Results

Thin film γ-$Cu_3V_2O_8$ photoanodes were deposited onto ITO-coated glass substrates by reactive magnetron co-sputtering, as described in the Methods section and ref. 30. The ITO-coated glass substrates were chosen for their relatively low surface roughness, which reduces scattering of the incident light and considerably simplifies the optical modeling. A cross sectional scanning electron microscopy (SEM) image of as-deposited γ-$Cu_3V_2O_8$ is shown in Fig. S1 (ESI†) and highlights the planar nature of the glass/ITO/γ-$Cu_3V_2O_8$ thin film stack. The wavelength-dependent optical constants for each layer were extracted by fitting of variable angle spectroscopic ellipsometry data, as described in the Methods section and the ESI.† These values were input into

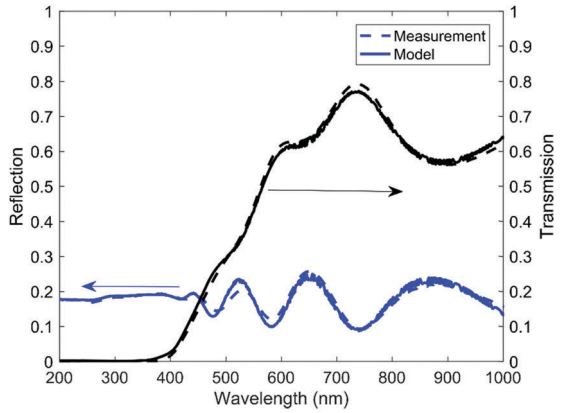

Fig. 1 Comparison of measured reflection and transmission spectra with those computed using the transfer matrix method with optical constants obtained from variable angle spectroscopic ellipsometry.

optical simulations based on the transfer matrix method (TMM) to determine photocarrier generation profiles as a function of wavelength within the photoactive γ-$Cu_3V_2O_8$ layer.[33] Multiple reflections in incoherent layers, such as the glass substrate and water layer, were accounted for using the phase elimination method.[34] As a first step, the validity of the simulation was tested by comparing the transmission and reflection spectra calculated with the TMM to transmission and reflection data collected in UV-Vis measurements. Fig. 1 shows the modeled and measured optical characteristics of the photoanode. The good agreement between the modeled and the experimentally measured UV-Vis data, along with the interference fringes observed in the measured spectra, indicate that light scattering effects are relatively small compared to specular reflection and transmission. This confirms that the optics of the system can be modeled adequately with the one-dimensional TMM model, which assumes perfectly flat surfaces.

Once the optical model was verified, the optical generation profile at each wavelength probed in the IPCE measurement was calculated. Next, the photoelectrochemical performance of the photoanodes was characterized by *J–E* and IPCE measurements in a 0.1 M sodium borate buffer electrolyte at pH 9.3. A three-electrode configuration, comprising a Pt wire as counter electrode, a Ag/AgCl electrode as reference, and the γ-$Cu_3V_2O_8$ thin film as working electrode, was used. Fig. 2(a) shows the measured front- and back-side illuminated IPCE spectra obtained at several operating potentials. All measurements were conducted with a white light bias incident from the front-side. The inset shows the *J–E* characteristics collected in the dark, as well as under the same front-side white-light bias that was used as the background illumination in the IPCE measurements. The vertical dotted lines correspond to the bias potentials at which IPCE measurements were subsequently conducted.

In order to extract $\phi(z)$ profiles that describe charge transport with minimal uncertainty at all positions, z, the two matrices describing the optical generation profiles with front- and back-side illumination were concatenated and so were the corresponding front- and back-illuminated IPCE spectra at every potential. The concatenated matrices and vectors were inserted into eqn (4) and the $\phi(z)$ profiles were extracted using a DSVD algorithm, as described in the Methods section and by Hansen.[32] Thus, every profile was extracted from both front-illuminated and back-illuminated IPCE measurements. Fig. 2(b) shows the resulting $\phi(z)$ profiles. Since the regions closest to the electrode surface are the most relevant for understanding mechanisms of energy conversion in these photoanodes, a view expanded to the first 30 nm is displayed. The inset in Fig. 2(b) is a full view of the curves. An elaborated discussion about the regularization procedure, spatial grid, and the regularization spread, which is a measure of the fluctuation of the extracted solutions with changing regularization parameter, can be found

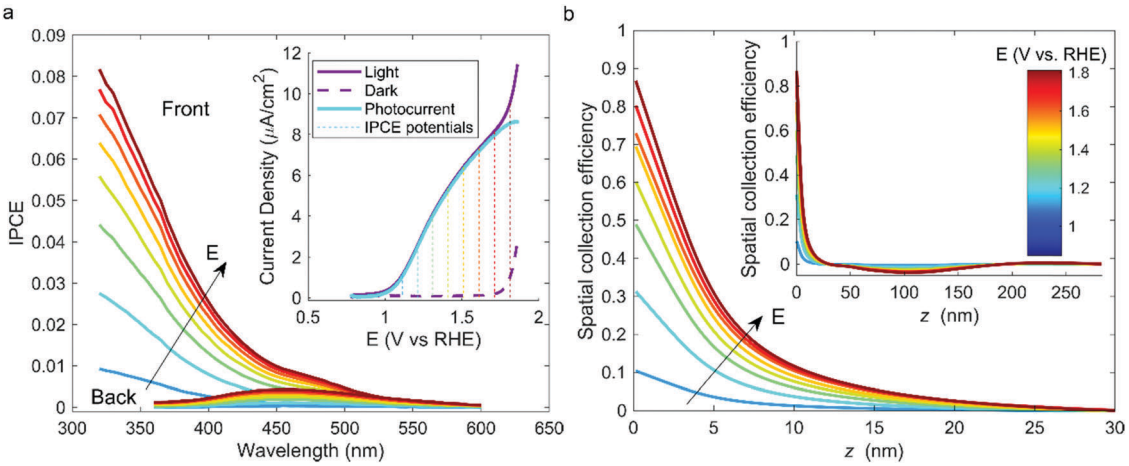

Fig. 2 $\phi(z)$ analysis of a γ-$Cu_3V_2O_8$ photoanode under water oxidation conditions. (a) Front- and back-side illuminated IPCE data acquired at different potentials. The inset shows current density *vs.* applied electrochemical potential (*J–E*) characteristics of the samples under white-light LED illumination (solid purple) and in the dark (dashed purple), along with the photocurrent (solid cyan) obtained by subtracting the dark from the illuminated data. The vertical dotted lines indicate the operating points at which IPCE measurements were performed. (b) The extracted $\phi(z)$ profiles are shown over the first 30 nm below the surface of the sample as a function of applied electrochemical potential. The inset provides a full view of the $\phi(z)$ profiles. The color coding for all IPCE and $\phi(z)$ curves in (a) and (b) represents the applied electrochemical potential, as given in the upper right of (b).

in the ESI.† The sharp decay in $\phi(z)$ agrees well with expectations for diffusion-limited photocurrent, in which the concentration of minority carriers decays with distance from the space charge region.[24,35–40] From Fig. 2(b), it can be seen that the vast majority of the collected carriers are those generated within the first 10 nm of the surface of the electrode, which is in good agreement with our prior work, in which the collection length was determined to be approximately 20–40 nm by analysis of film thickness-dependent photocurrents.[30]

In order to better understand the change in surface reactivity with potential, the SCE analysis was also applied to IPCE measurements conducted using a sacrificial reagent. An identically deposited and processed γ-$Cu_3V_2O_8$ sample was measured in 0.1 M sodium borate buffer electrolyte (pH 9.3) containing 0.1 M Na_2SO_3 as a sacrificial hole acceptor. Fig. 3(a) shows the measured IPCE spectra obtained under front-side and back-side illumination at several operating potentials. As above, these spectra were used as inputs to the regularization problem, such that every front- and back-illuminated IPCE spectra produced a single SCE profile describing the transport characteristics of the system at the corresponding potential. The $\phi(z)$ in the region near the surface are shown in Fig. 3(b) and the inset shows the complete profile over the full thickness of the sample. Similar to the profiles extracted under water splitting conditions, the $\phi(z)$ profiles shows a rapidly decaying collection efficiency in which nearly all collected charge carriers originate from within the first 10 nm of the surface. However, since the reaction kinetics in the presence of sacrificial hole acceptor are much faster than for water oxidation, the surface reactivity, ϕ_s, is significantly larger at lower potentials.

The bulk performance of the photoanode as a light capture material is mainly determined by the minority carrier collection length, L_c, which is the distance from the surface over which photogenerated charge carriers can be efficiently extracted to contribute to the current. The collection length comprises two components: a diffusion component, which is independent of the applied potential, and a drift component, which increases with potential as the thickness of the space charge region under the semiconductor/electrolyte interface increases. Here, we define the collection length as the distance from the surface at which ϕ_b reaches 0.1. As discussed above, in minority carrier limited photoanodes, ϕ_b is 1 at the surface ($z = 0$). Thus, the collection length is also given by the distance at which the SCE reaches 0.1 of its value at the surface, *i.e.* $\phi(L_c) = 0.1\phi(0)$. Fig. 4 shows the collection lengths extracted from SCE profiles as a function of the applied potential. The filled data points correspond to measurements performed with a sacrificial reagent and the open points show data obtained under water splitting conditions in the absence of sacrificial reagent. The error bars indicate the uncertainty imposed by the regularization spread, as discussed in the ESI.† Different samples, deposited and processed under nominally identical conditions, were measured and are indicated by the different shapes of the data points. The inset shows the photocurrent change with potential with and without sacrificial reagent, and corresponds to the data presented in the insets of Fig. 2 and 3. In all cases, the collection length is between 9 and 13 nm and increases with applied potential. However, the modest increase in collection length – of ~2 nm over the investigated potential range – indicates that the primary impact of the applied anodic potential on photocurrent density from γ-$Cu_3V_2O_8$ photoanodes (see inset) is to improve charge extraction across the interface rather than to increase the thickness of the space charge region. This weak dependence of the space charge thickness on applied electrochemical potential is in contrast to ideal models of well-behaved semiconductor photoelectrodes, as discussed below.[41] It should be noted that changes in the collection length due to the addition of a sacrificial reagent are below the sensitivity of the method,

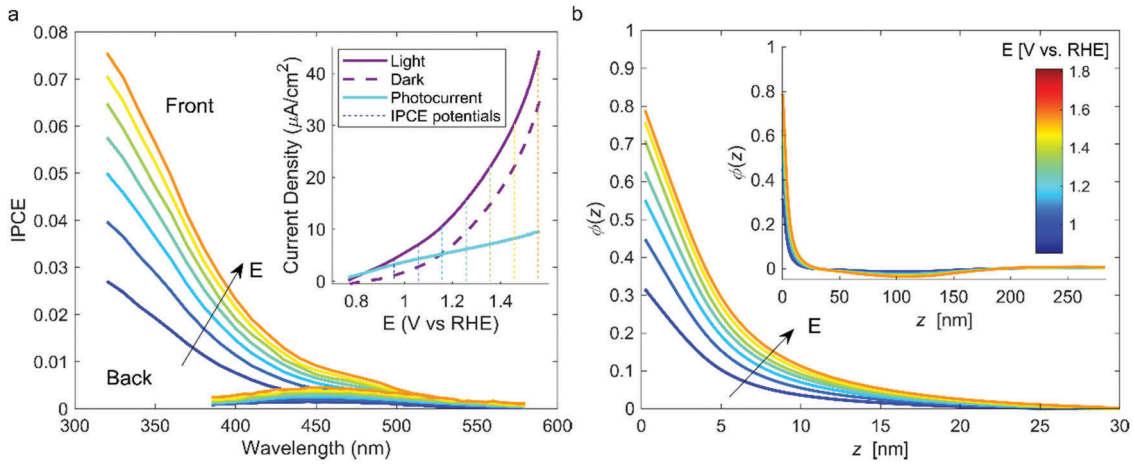

Fig. 3 $\phi(z)$ analysis of a γ-$Cu_3V_2O_8$ photoanode in the presence of a sacrificial hole acceptor. (a) Front- and back-side IPCE measurements acquired at different potentials in the presence of 0.1 M Na_2SO_3 as sacrificial hole acceptor. The inset shows current density *vs.* applied electrochemical potential (J–E) characteristics of the samples under white-light LED illumination (solid purple) and in the dark (dashed purple), along with the photocurrent (solid cyan) obtained by subtracting the dark from the illuminated data. The vertical dotted lines indicate the operating points at which IPCE measurements were performed. (b) The extracted $\phi(z)$ profiles are shown over the first 30 nm below the surface of the sample as a function of applied electrochemical potential. The inset provides a full view of the $\phi(z)$ profiles. The color coding with respect to the applied potential is the same as in Fig. 2.

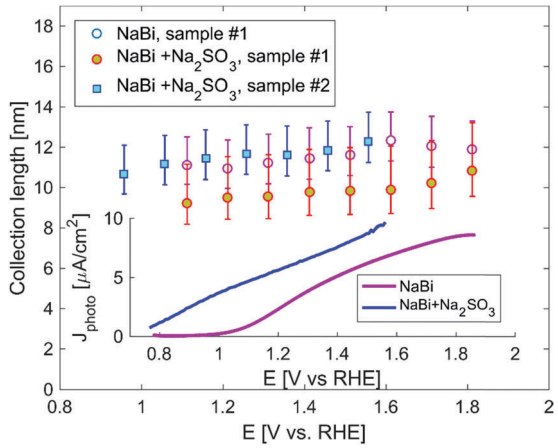

Fig. 4 The collection length as a function the operating potential. The filled markers are for measurements with a sacrificial reagent and the open markers are for measurements under water splitting conditions. The markers' shapes denote different samples that were analyzed. The error bars indicate the uncertainty in the collection length due to the regularization spread. The inset shows the photocurrent as a function of applied electrochemical potential, corresponding to data in the insets of Fig. 2 and 3.

which in the present case is on the order of ±1 nm (see error bars in Fig. 4 and discussion in the ESI† regarding errors imposed by the regularization spread). The collection lengths with and without a sacrificial reagent are practically identical, even at low potentials where fast redox processes increase the photocurrent dramatically. This implies that the addition of a sacrificial reagent does not increase the band banding near the surface but instead reduces recombination at the surface. This is a consequence of fast scavenging of holes from the surface, which in turn reduces the population of hole-occupied surface states.

The thickness of the space charge region can be estimated *via* Mott–Schottky analysis, in which the capacitance of the space charge region is measured as a function of potential by electrochemical impedance spectroscopy.[42] Although the permittivity of γ-$Cu_3V_2O_8$ is not yet known, the value can be approximated to be on the order of that in hematite, which is also a polar charge transfer insulator. Under this assumption, we find that the active donor concentration is on the order of 10^{19} cm^{-3}. According to established models of semiconductor depletion and as discussed in ref. 42, such high donor concentrations limit the width of the space charge region to be on the order of 10–20 nm, which agrees well with the collection lengths derived in this work. Additional details about the Mott–Schottky analysis can be found in the ESI.† An alternative explanation for weak dependence of the collection length with potential may be because of Fermi level pinning at the semiconductor/electrolyte interface. In such case, some of the applied potential will be forced to drop over the Helmholtz layer rather than within the semiconductor. Further work is required in order to quantify the relative contributions from the two mechanisms.

In this work, the collection length was defined as the distance in which $\phi_b(z)$ reaches a value of 0.1. We note that an intuitive definition for the collection length may be the distance in which $\phi_b(z)$ is $1/e$ (0.37), which corresponds to an exponential fit of the form $\phi(z) = \phi_s \exp(-z/L_c)$.[43] However, this type of analysis requires prior knowledge on the width of the space charge region and assumes 100% collection for charge carriers in it, thus making it inappropriate for material system described in this work. Development of the detailed theory that describes the expected collection efficiency profiles is left for future work.

The overall fraction of charge carriers collected, lost to surface recombination, and lost through bulk recombination ($\bar{\phi}$, $\bar{R}_s$, and $\bar{R}_b$, respectively) can be analyzed by inserting the extracted $\phi(z)$ profiles into eqn (5)–(8). Fig. 5(a) shows the integrated fraction of collected photocarriers along with the fractions of those lost within the bulk and at the surface, as a function of the applied potential. Here, the fraction of charge carriers collected ($\bar{\phi}$) is calculated with eqn (8), the fraction of charge carriers lost to bulk recombination is given by $\bar{R}_b = 1 - \bar{\phi}_b$, where $\bar{\phi}_b$ is determined using eqn (6), and the fraction of charge carriers lost through surface recombination ($\bar{R}_s$) is calculated using eqn (7). The incident illumination is assumed to be the AM 1.5G solar spectrum and the SCE profiles were taken from Fig. 2(b). As seen in Fig. 5(a), for the entire potential range tested, more than 98% of the absorbed charge carriers are lost through bulk recombination, indicating that poor photocarrier transport properties form the main performance bottleneck for this material. As shown in Fig. 2–4, the charge collection efficiency is very low beyond approximately 10 nm from the surface. This charge extraction length is highly mismatched to the optical absorption depth within the visible and near-UV range.[30] Thus, the vast majority of photocarriers are generated deep within the bulk of the photoanode and recombine before extraction is possible. Such a mismatch between charge extraction length and optical absorption depth is common among transition metal oxide semiconductors and there are several approaches for reducing the bulk losses in such materials. Reducing the distance minority carriers must travel before reaching the surface can be accomplished by nanostructuring[44] or by applying resonant light trapping techniques that increase the optical generation near the surface.[45] Both approaches were demonstrated and have been shown to be quite effective in hematite, which possesses similar transport properties. A complementary approach is to increase the collection length within the material. In the present case, reducing the majority carrier density through defect engineering of the films would be a first strategy for increasing the extent of the space charge region and its evolution with applied anodic potential. Similarly, passivation of defects and creation of homo- and hetero-junctions that increase the thickness of the space charge region may be viable approaches for mitigating bulk losses.[46,47] However, understanding the fundamental processes that define the minority carrier diffusion length (*e.g.* recombination and trapping at defects, self-trapping of holes, polaronic transport, *etc.*) will be essential for determining intrinsic limits to transport and devising strategies to most efficiently address them.

Recombination events at the semiconductor/electrolyte interface are facilitated by minority carriers trapped at the surface and majority carriers that are injected towards the surface over

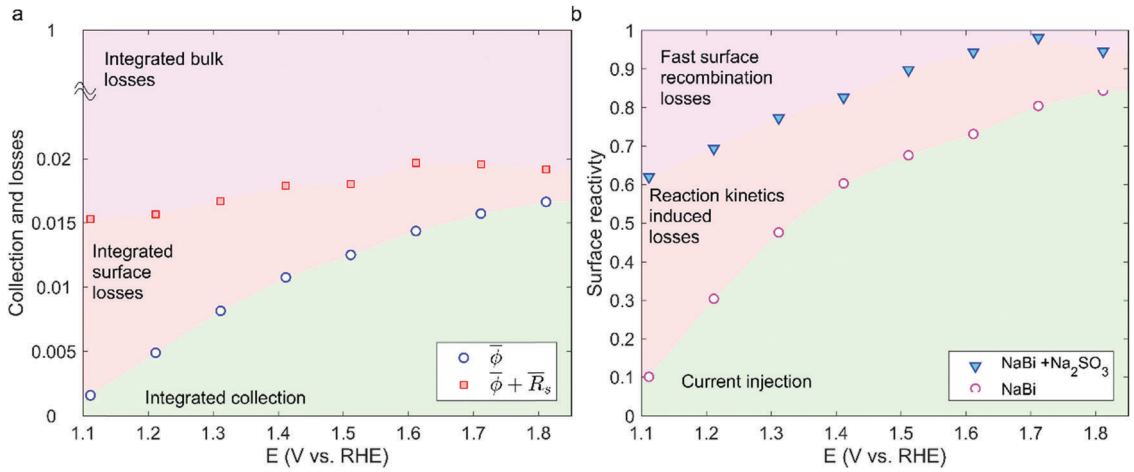

Fig. 5 Loss quantification for γ-$Cu_3V_2O_8$ photoanodes. (a) The integrated collection, surface losses, and bulk losses as a function of the applied potential. The optical generation profile is based on the AM 1.5G spectrum and the $\phi(z)$ profiles are taken from Fig. 2. (b) The surface reactivity as a function of potential with and without a sacrificial reagent allow fast recombination losses to be discriminated from those arising due to slow reaction kinetics.

or through the potential barrier at the semiconductor/electrolyte interface. For example, intermediate species associated with the chemical reaction can trap photogenerated holes at the surface.[48] Another recombination pathway is through electronically active defect states near the surface, a process that is also known to reduce the performance of solid state photovoltaic devices.[49] In both cases, the steady state that is reached includes injection of electrons into the charged defects or intermediate states. Thus, the number of recombination events at the surface is determined by the rate constant for this process and the concentration of electrons and holes near the surface. Surface recombination losses can be divided to two types of losses according to their characteristic timescales compared to the reaction rate in the presence of a sacrificial reagent. Surface recombination processes through intermediate states have been shown to be much slower than the oxidation of sacrificial reagents.[10] As a result, these can be probed experimentally by comparing the photoanode performance in the presence and absence of a sacrificial reagent.[10] On the other hand, recombination events that are significantly faster than the reaction kinetics with a sacrificial reagent will be present with a sacrificial reagent and without it. This type of classification implies that slow recombination events can be suppressed by incorporating a catalyst that accelerates the reaction kinetics. However, it is difficult to expect that the reaction rate introduced by a catalyst will surpass the oxidation rate of sacrificial reagents. For this reason, the surface losses in the presence of a sacrificial reagent set an upper limit to the performance of a catalyst-integrated photoelectrode. Further suppression of surface losses must be done through removal of the states that trap minority carriers, or by blocking majority carriers from reaching the surface. These processes are usually referred to as surface passivation.[50] In the following paragraph these two types of surface losses are studied by analyzing the SCE at the surface ($z = 0$) at several operating potentials in the presence and absence of a sacrificial reagent.

The fraction of carriers at the surface that contribute to current, which we define as the surface reactivity, can be studied by plotting how ϕ_s changes with potential. Fig. 5(b) shows the surface reactivity, which is defined as the extracted SCE at $z = 0$, as a function of potential with and without a sacrificial reagent. In the presence of a sacrificial reagent, as under water oxidation conditions, the increase in surface reactivity with potential is due to a combination of reduced surface recombination and increased reaction kinetics. The reduction in recombination may be a result of the band bending near the surface, which leads to a depletion of majority electrons, as expected and observed in α-Fe_2O_3 water splitting photoanodes.[51] At highly anodic potentials, the surface is almost completely depleted and the surface reactivity saturates to a value just below 1. The surface reactivity under water oxidation conditions (*i.e.* in the absence of sacrificial hole acceptor) is significantly lower than the surface reactivity in the presence of a sacrificial reagent over the entire potential range tested. Assuming that the only role of the sacrificial hole acceptor is to enhance reaction kinetics, the difference in surface reactivity obtained with and without the sacrificial reagent provides an indication of losses inflicted by slow water oxidation kinetics. Hence, the branching ratio between charge injection, fast surface recombination through defect states, and slow recombination processes due to slow reaction kinetics can be deduced, as indicated by the colored regions in Fig. 5(b).

It should be noted that the fast surface recombination events are not directly probed by frequency domain techniques or transient photocurrent spectroscopy. In addition, it is often assumed that surface recombination losses are completely eliminated when sacrificial hole acceptor is present in the solution. Our findings indicate that this is not the case and provide a means of quantifying these non-negligible recombination losses even in the presence of fast redox processes. Such surface recombination losses are often overlooked or mistakenly grouped with bulk losses.[10,11] Identifying the origin of the recombination

processes is critical for understanding efficiency loss mechanisms and developing strategies for overcoming them. For example, for systems exhibiting considerable fast surface recombination losses, surface passivation and control of interfacial defects is likely to be more important for advancing efficient function than enhancing the catalytic activity.

Discussion

The transport properties and loss mechanisms of γ-$Cu_3V_2O_8$ photoanodes were studied and quantified by extraction of charge collection efficiency profiles under different operating potentials and in the presence and absence of a sacrificial hole acceptor. Although the results obtained here are specific to γ-$Cu_3V_2O_8$, the extraction method is based on generic techniques: optical modeling and IPCE (EQE) measurements. This allows for extension of this characterization method to a wide range of new semiconductors and assemblies, thus enabling rapid, yet in-depth, understanding of the transport properties and performance bottlenecks in new and emerging materials for solar energy harvesting. In addition, while the SCE extraction method presented here assumes that the tested sample is flat and uniform in composition, there are significant opportunities for extending this approach to heterogeneous or nanostructured electrodes. For example, this may be accomplished by applying the method to ordered, periodic micro- or nanostructures with defined geometries and symmetries. Further development of the SCE approach to nanoscale transport probes can elucidate the effects of different surfaces and interfaces in more complex nanostructured systems.

Detailed understanding of the collection efficiency profile and its potential dependence is an important step in accelerating material and device optimization to improve efficiency. As discussed above, the first step towards increasing the photocurrent in the tested γ-$Cu_3V_2O_8$ photoanodes is to reduce bulk losses by increasing the collection length. Mott–Schottky analysis indicates that the active donor concentration is very high and explains the very short collection length and its small increase with potential. Hence, reducing the donor concentration by, for example, tuning deposition conditions, post-growth thermal annealing in controlled gas environments, or introducing compensating impurities may have a dramatic effect on improving performance.

Distinguishing between fast surface recombination losses and losses induced by slow reaction kinetics, as well as quantifying their relative contributions, is expected to shed important new light on the role of catalysts in the function of semiconductor photoelectrodes.[13] In recent years, it has become increasingly apparent that the incorporation of a catalyst layer on a semiconductor can improve efficiency *via* a combination of several different mechanisms, including by increasing reaction kinetics, passivating surface states, and increasing band bending to provide a wider space charge region. The relative contribution of each mechanism depends on the specific materials combination, deposition conditions, and operating environment. Application of the method and analysis reported here is expected to help discriminate between these factors and elucidate the various roles played by the catalyst layer. For example, passivation of electronically charged defects at the electrode surface is expected to increase the surface reactivity in the presence of a sacrificial reagent. On the other hand, increased band bending is expected to increase the collection length and the surface reactivity as the surface becomes depleted of majority carriers. Such improved understanding of the role of overlayers, engineered interfaces, and catalysts will allow targeted strategies to improve photoelectrochemical performance characteristics.

Conclusions

The spatial charge collection efficiency profiles of γ-$Cu_3V_2O_8$ were extracted by combining optical modeling and IPCE measurements at different potentials. It was shown that the vast majority of the charge carriers are collected within 10 nm of the electrode surface and that the collection length increases weakly with the applied potential. However, the surface reactivity was shown to increase with potential, indicating that the primary mechanism by which current increases with potential is a result of reduced surface recombination rather than increased space charge thickness. By comparing the surface reactivity in the presence and absence of a sacrificial reagent, we were able to distinguish between losses attributed to fast recombination at surface defects and additional losses induced by slow reaction kinetics. Importantly, these results indicate that complete suppression of surface recombination cannot be assumed when a sacrificial reagent is present. Finally, it was shown that under 1 sun conditions approximately 98% of the photogenerated charge carriers in γ-$Cu_3V_2O_8$ are lost to bulk recombination. The mechanistic information provided by this new *operando* characterization method allows all the losses within the device to be determined and enables clear guidelines for photoanode optimization to be established. In the present case, reducing surface recombination by interface engineering and reducing bulk doping by defect engineering are expected to significantly increase the functional performance of γ-$Cu_3V_2O_8$ photoanodes. More generally, applying this method to new materials may help accelerate their evaluation as promising candidate replacements for existing semiconductors and aid their development as components in high performance solar energy harvesting systems.

Conflicts of interest

There are no conflicts to declare.

Acknowledgements

This material is based upon work performed by the Joint Center for Artificial Photosynthesis, a DOE Energy Innovation Hub, supported through the Office of Science of the US Department of Energy under Award Number DE-SC0004993. We gratefully acknowledge useful scientific discussions with Avner Rothschild, Hen Dotan, Dino Klotz, Daniel Grave and David Ellis

from the Department of Materials Science and Engineering, Technion, Israel.

References

1 K. Sivula and R. van de Krol, *Nat. Rev. Mater.*, 2016, 15010.
2 I. D. Sharp, J. K. Cooper, F. M. Toma and R. Buonsanti, *ACS Energy Lett.*, 2017, **2**, 139–150.
3 J. Sinkkonen, J. Ruokolainen, P. Uotila and A. Hovinen, *Appl. Phys. Lett.*, 1995, **66**, 206–208.
4 E. Tuominen, M. Acerbis, A. Hovinen, T. Siirtola and J. Sinkkonen, *Phys. Scr.*, 1997, **T69**, 306–309.
5 Y. T. Pang, H. Efstathiadis, D. Dwyer and M. D. Eisaman, *2015 IEEE 42nd Photovolt. Spec. Conf.*, 2015, 15–18.
6 C. Donolato, *J. Appl. Phys.*, 2001, **89**, 5687–5695.
7 C. Donolato, *Appl. Phys. Lett.*, 1999, **75**, 4004–4006.
8 C. Donolato, *J. Appl. Phys.*, 1991, **69**, 7287–7294.
9 G. Segev, H. Dotan, D. S. Ellis, Y. Piekner, D. Klotz, J. W. Beeman, J. K. Cooper, D. A. Grave, I. D. Sharp and A. Rothschild, *Joule*, DOI: 10.1016/J.JOULE.2017.12.007.
10 H. Dotan, K. Sivula, M. Grätzel, A. Rothschild and S. C. Warren, *Energy Environ. Sci.*, 2011, **4**, 958.
11 D. K. Zhong, S. Choi and D. R. Gamelin, *J. Am. Chem. Soc.*, 2011, **133**, 18370–18377.
12 F. Le Formal, S. R. Pendlebury, M. Cornuz, S. D. Tilley, M. Grätzel and J. R. Durrant, *J. Am. Chem. Soc.*, 2014, **136**, 2564–2574.
13 K. Sivula, *J. Phys. Chem. Lett.*, 2013, **4**, 1624–1633.
14 K. G. Upul Wijayantha, S. Saremi-Yarahmadi and L. M. Peter, *Phys. Chem. Chem. Phys.*, 2011, **13**, 5264–5270.
15 L. M. Peter, K. G. U. Wijayantha and A. A. Tahir, *Faraday Discuss.*, 2012, **155**, 309–322.
16 D. Klotz, D. S. Ellis, H. Dotan and A. Rothschild, *Phys. Chem. Chem. Phys.*, 2016, **18**, 23438–23457.
17 B. Klahr, S. Gimenez, F. Fabregat-Santiago, T. Hamann and J. Bisquert, *J. Am. Chem. Soc.*, 2012, **134**, 4294–4302.
18 R. K. Ahrenkiel, *Solid-State Electron.*, 1992, **35**, 239–250.
19 B. C. Connelly, G. D. Metcalfe, H. Shen and M. Wraback, *Appl. Phys. Lett.*, 2010, **97**, 251117.
20 E. Edri, S. Kirmayer, A. Henning, S. Mukhopadhyay, K. Gartsman, Y. Rosenwaks, G. Hodes and D. Cahen, *Nano Lett.*, 2014, **14**, 1000–1004.
21 N. Kedem, T. M. Brenner, M. Kulbak, N. Schaefer, S. Levcenko, I. Levine, D. Abou-Ras, G. Hodes and D. Cahen, *J. Phys. Chem. Lett.*, 2015, **6**, 2469–2476.
22 C. M. Sutter-Fella, J. A. Stückelberger, H. Hagendorfer, F. La Mattina, L. Kranz, S. Nishiwaki, A. R. Uhl, Y. E. Romanyuk and A. N. Tiwari, *Chem. Mater.*, 2014, **26**, 1420–1425.
23 L. Kranz, C. Gretener, J. Perrenoud, R. Schmitt, F. Pianezzi, F. La Mattina, P. Blösch, E. Cheah, A. Chirilă, C. M. Fella, H. Hagendorfer, T. Jäger, S. Nishiwaki, A. R. Uhl, S. Buecheler and A. N. Tiwari, *Nat. Commun.*, 2013, **4**, 2306.
24 R. A. Pala, A. J. Leenheer, M. Lichterman, H. A. Atwater and N. S. Lewis, *Energy Environ. Sci.*, 2014, **7**, 3424–3430.
25 J. A. Seabold and N. R. Neale, *Chem. Mater.*, 2015, **27**, 1005–1013.
26 L. Zhou, Q. Yan, A. Shinde, D. Guevarra, P. F. Newhouse, N. Becerra-Stasiewicz, S. M. Chatman, J. A. Haber, J. B. Neaton and J. M. Gregoire, *Adv. Energy Mater.*, 2015, **5**, 1500968.
27 Q. Yan, J. Yu, S. K. Suram, L. Zhou, A. Shinde, P. F. Newhouse, W. Chen, G. Li, K. A. Persson, J. M. Gregoire and J. B. Neaton, *Proc. Natl. Acad. Sci. U. S. A.*, 2017, **114**, 3040–3043.
28 W. Guo, W. D. Chemelewski, O. Mabayoje, P. Xiao, Y. Zhang and C. B. Mullins, *J. Phys. Chem. C*, 2015, **119**, 27220–27227.
29 D. Hayes, R. G. Hadt, J. D. Emery, A. A. Cordones, A. B. F. Martinson, M. L. Shelby, K. A. Fransted, P. D. Dahlberg, J. Hong, X. Zhang, Q. Kong, W. Schoenlein and L. X. Chen, *Energy Environ. Sci.*, 2016, **9**, 3754–3769.
30 C.-M. Jiang, M. Farmand, C. H. Wu, Y.-S. Liu, J. Guo, W. S. Drisdell, J. K. Cooper and I. D. Sharp, *Chem. Mater.*, 2017, **29**, 3334–3345.
31 A. N. Tikhonov, A. V. Goncharsky, V. V. Stepanov and A. G. Yagola, *Numerical Methods for the Solution of Ill-Posed Problems*, 1995.
32 P. C. Hansen, *Numer. Algorithms*, 2007, **46**, 189–194.
33 G. F. Burkhard, E. T. Hoke and M. D. McGehee, *Adv. Mater.*, 2010, **22**, 3293–3297.
34 A. Campa, J. Krc and M. Topic, *Prog. Electromagn. Res.*, 2013, **137**, 187–202.
35 B. Ali, R. Murray, S. S. Hegedus and S. Ismat Shah, *J. Appl. Phys.*, 2012, **112**, 114514.
36 A. E. Delahoy, Z. Cheng and K. K. Chin, *27th Eur. Photovolt. Sol. Energy Conf. Exhib.*, 2012, 2837–2842.
37 C. J. Hages, N. J. Carter and R. Agrawal, *J. Appl. Phys.*, 2016, **119**, 14505.
38 S. S. Hegedus, *Prog. Photovoltaics Res. Appl.*, 1997, **5**, 151–168.
39 X. X. Liu and J. R. Sites, *J. Appl. Phys.*, 1994, **75**, 577–581.
40 S. Hegedus, D. Desai and C. Thompson, *Prog. Photovoltaics Res. Appl.*, 2007, **15**, 587–602.
41 W. W. Gärtner, *Phys. Rev.*, 1959, **116**, 84–87.
42 R. Van De Krol, *Photoelectrochemical Hydrogen Production*, 2012, pp. 13–67.
43 M. A. Green, *Solar Cells: Operating Principles, Technology, and System Applications*, 1982.
44 S. C. Warren, K. Voïtchovsky, H. Dotan, C. M. Leroy, M. Cornuz, F. Stellacci, C. Hébert, A. Rothschild and M. Grätzel, *Nat. Mater.*, 2013, **12**, 842–849.
45 H. Dotan, O. Kfir, E. Sharlin, O. Blank, M. Gross, I. Dumchin, G. Ankonina and A. Rothschild, *Nat. Mater.*, 2013, **12**, 158–164.
46 F. F. Abdi, L. Han, A. H. M. Smets, M. Zeman, B. Dam and R. van de Krol, *Nat. Commun.*, 2013, **4**, 2195.
47 J.-W. Jang, C. Du, Y. Ye, Y. Lin, X. Yao, J. Thorne, E. Liu, G. McMahon, J. Zhu, A. Javey, J. Guo and D. Wang, *Nat. Commun.*, 2015, **6**, 7447.
48 L. M. Peter and D. Vanmaekelbergh, *Adv. Electrochem. Sci. Eng.*, 2008, **6**, 77–163.
49 P. Wurfel, *Physics of Solar Cells from Principles to New Concepts*, Wiley, 2005.
50 O. Zandi and T. W. Hamann, *J. Phys. Chem. Lett.*, 2014, **5**, 1522–1526.
51 K. G. Upul Wijayantha, S. Saremi-Yarahmadi and L. M. Peter, *Phys. Chem. Chem. Phys.*, 2011, **13**, 5264.

